Nonlinear reverberation spectroscopy with phase-sensitive superheterodyne reception*

Ward L. Johnson

Applied Chemicals and Materials Division, National Institute of Standards and Technology, 325 Broadway, Boulder, CO 80305

Abstract

A technique is presented for determining elastic nonlinearity of materials from resonant frequency shifts as a function of signal amplitude during free vibrational decay after tone-burst excitation. The technique differs from previous nonlinear reverberation spectroscopy (NRS) techniques in that it employs phase-sensitive superheterodyne reception. Time-dependent amplitudes of in-phase and out-of-phase components of signals, relative to a reference sinusoid at the excitation frequency, are provided through analog hardware processing in the absence of digitization of the signal from the vibrational sensor. The time-dependent phase and amplitude of the signal are determined through software analysis of these in-phase and out-of-phase components, and the instantaneous frequency during free decay is then determined from the time derivative of the phase. With this approach, superheterodyne reception and low-pass filtering of the phase-detector outputs lead to a great reduction in noise and computation effort, relative to direct digitization and software processing of the sensor signal, while retaining information on frequency shifts on a relevant time scale during ringdown. As with other NRS techniques, rapid acquisition of data on amplitude dependence of the resonant frequency during ringdown leads to minimization of systematic errors from temperature drift. The technique is demonstrated with noncontacting electromagnetic-acoustic transduction on custom alloyed Al (0.2 at.% Zn) and commercial Al 7075 cylinders with axial-shear resonant frequencies between 658 kHz and 659 kHz. The precision of measurements of relative

frequency shifts is found to be on the order of 0.1 parts per million (ppm), exceeding by two orders of magnitude the best reported precision of nonlinear resonant ultrasound spectroscopy (NRUS).

Keywords: acoustic nonlinearity, acoustic resonance, amplitude dependence, electromagnetic-acoustic transduction, EMAT, electromagnetic-acoustic resonance, EMAR, nonlinear reverberation spectroscopy, NRS, ultrasonics

1. Introduction

Nonlinear elastic measurements can be much more effective than linear elastic measurements at detecting a variety of microscale and nanoscale features in materials, including cracks, delaminations, dislocations, and precipitates [1, 2, 3, 4, 5, 6]. As a consequence of this sensitivity, the development and application of nonlinear acoustic techniques have been extensively pursued in recent decades, especially in the context of nondestructively sensing the presence and characteristics of flaws that affect the mechanical integrity of metals, concrete, rock, bone, and composites [6, 7]. These techniques include nonlinear resonant ultrasound spectroscopy (NRUS) [8], harmonic evolution of propagating waves (most commonly second-harmonic generation, SHG [7]), generation of spectral side bands from nonlinear frequency mixing (including nonlinear wave modulation spectroscopy (NWMS) [9]), "vibroacoustic" mixing of high- and low-frequency excitations (VAM) [10], amplitude modulation of high-frequency excitation (MHF) [11], and time-domain nonlinear reverberation spectroscopy (NRS) [12, 13].

Each of these nonlinear measurement techniques has relative advantages and disadvantages with respect to sensitivity, range of applicability, ease/speed of use, specific information provided, and precision. For example, currently established techniques that employ propagating waves are limited to specimens with regular (*e.g.*, planar or cylindrical) geometries and are complicated by effects of frequency-dependent attenuation and diffraction, if focused on harmonic or subharmonic generation [14]. Resonance techniques, while applicable to any geometry, are insensitive to defects located at nodal points of the acoustic stress pattern (if a single mode is employed), and temperature drift and associated shifts in resonant-frequency during acquisition of swept-frequency spectra introduce uncertainties in measurements of peak frequencies. Techniques that measure only one factor in the nonlinear stress-strain

relation (*e.g.*, quadratic nonlinearity) can be relatively insensitive to some types of defects [6, 15].

Although less widely employed, NRS offers an advantage over swept-frequency resonance techniques with respect to temperature drift during data acquisition, because measurements are much more rapid. Previously developed NRS techniques have employed various approaches for measuring nonlinear shifts in resonant frequency as a function of vibrational amplitude during free decay following excitation with a driving tone burst. Each of these approaches begins with acquisition of signal voltages that are proportional to vibrational displacement as a function of time. The signal is then analyzed to determine the instantaneous resonant frequency as a function of signal amplitude during the decay. Methods of performing this analysis include (1) successive fitting of the signal to a decaying sinusoid in a series of small time windows, with the frequency, log decrement, and phase offset as adjustable fit parameters [12], (2) successive Fourier transforms in a series of small time windows [16], (3) evaluation of zero crossings of the signal [17, 18], and (4) derivatives of phase extracted from a Hilbert transform [19]. The application of these methods has focused primarily on flexural modes at audio or sub-audio frequencies (less than a few tens of kHz), with an exception in the work of Polunin *et al.* [20] on MEMS resonances at 1.2 MHz.

This paper presents an NRS technique that employs hardware extraction of the time-dependent amplitude of the in-phase and out-of-phase components of the signal, relative to the phase of a reference sinusoid that is gated to produce the driving tone burst. With respect to signal processing, the hardware system is functionally similar to a lock-in amplifier but, additionally, employs superheterodyne reception to increase signal-to-noise ratios. The instantaneous frequency is determined from the time derivative of the phase, which is determined from the amplitudes of the out-of-phase and in-phase components of the signal. With hardware extraction of these amplitudes, demands on digitization speed and computational effort are greatly reduced, relative to direct digitization and analysis of the decaying signal at the time-dependent resonant frequency. An additional feature of the specific implementation presented here is noncontacting electromagnetic-acoustic transduction, which eliminates systematic errors associated with contacting transducers. This implementation is a nonlinear time-domain variant of electromagnetic-acoustic resonance, EMAR.

This work is partly motivated by an industrial need for rapid nondestructive evaluation (NDE) of additively manufactured (AM) alloys with complex

part geometries. In this context, the objective is detection of microstructural features that adversely affect mechanical performance, such as porosity, cracks, unintended precipitates, excessive residual stress, and excessive dislocation density. The basic measurement approach presented here was previously employed, with some differences in the method of analysis, to demonstrate correlations of nonlinearity with porosity in additively manufactured stainless steel [21]. This paper presents the technique with exemplary 658 kHz waveforms obtained from conventionally manufactured aluminum specimens. Although the presentation is focused on ultrasonic resonance of metal specimens, the general method of hardware and software processing is applicable to other types of nonlinear physical systems involving resonant ringdown after tone-burst excitation.

2. Specimens

Two cylindrical aluminum specimens are employed in this study. One specimen, denoted Al-Zn, is a custom cast alloy of aluminum containing 0.2 at.% Zn (Kamis, Inc.[1]), with each of the two constituent elements 99.999% pure. This specimen was turned on a lathe to a diameter of (8.0060 ± 0.0008) mm and a length of (26.067 ± 0.006) mm. A second specimen, denoted Al-7075, was turned on a lathe from a commercially manufactured 7075-T6 extruded aluminum rod with an initial diameter of 1.59 cm (5/8 inch). The machined diameter of this specimen is (7.996 ± 0.002) mm, and the length is (26.06 ± 0.002) mm. Measurements of the alloy composition of this specimen were not performed. For the purposes of this study, it is only necessary to note that standard concentrations of alloying elements in 7075 aluminum are in the range (5.1–6.1) wt% Zn, (2.1–2.9) wt% Mg, (1.2–2.0) wt% Cu, 0.5 wt% Fe, 0.4 wt% Si, 0.3 wt% Mn, (0.18–0.28) wt% Cr, and 0.2 wt% Ti [22]. From the measured dimensions and weights, the densities of Al-Zn and Al-7075 were determined to be (2694 ± 1) kg/m^3 and (2792 ± 2) kg/m^3, respectively. The 3.6 % difference in density is attributed primarily to the heavier alloying elements Zn and Cu in Al-7075.

The selection of these two specimens was motivated partly by an interest in including materials with much different levels of nonlinearity. Specimen Al-Zn, with a total impurity concentration comparable to commercially pure

[1]Identification of commercial products in this document is provided for technical completeness and does not reflect an endorsement by NIST.

aluminum, is expected to have relatively weak pinning of dislocations and, therefore, a substantial dislocation contribution to nonlinearity. The much greater concentration of alloying elements in Al-7075 is expected to provide relatively strong dislocation pinning and correspondingly lower nonlinearity. As described below, the data from this specimen with low nonlinearity also provide information on the resolution limit of the measurements.

3. Hardware

3.1. Excitation coil and magnetic field

A simple solenoid coil is employed here for electromagnetic-acoustic transduction. The coil is wound from 32-gauge magnet wire (0.257 mm diameter, including insulating varnish) on a Bakelite tube with an outer diameter of (9.50 ± 0.02) mm and a wall thickness of (0.57 ± 0.07) mm. The coil has 153 turns, a length of (41.0 ± 0.5) mm, and an inner diameter of (9.58 ± 0.02) mm, with low-conductivity tape between the coil and tube. As depicted in Fig. 1, a cylindrical specimen is inserted in the tube and supported by the inside surface of the tube with its principal axis $\hat{z}$ horizontal and parallel to the axis of the coil.

A static magnetic induction field $\mathbf{B}_0$ is introduced by an 8-segment cylindrical Halbach magnet (Magnetic Solutions Ltd., Dublin) with an inner diameter of (5.4 ± 0.1) cm. The direction of the magnetic field is horizontal and perpendicular to $\hat{z}$, as shown in Fig. 1. The magnitude of this field is 0.540 ± 0.005 T over the spatial region occupied by the coil and sample.

3.2. Electronic configuration

The coil is driven by a tone burst generated by a gated amplifier (RITEC Inc., Model RAM-5000 SNAP). This instrument internally generates a programmable sine wave that is gated to a user-specified burst width and amplified to a user-specified power level. The burst is set to have a nominal width of 2.6 ms and nominal repetition period of 2.0 s. The instrument slightly adjusts the set burst width to be an integral number of cycles and adjusts the timing and repetition period of the burst such that the beginning and end of the burst are at a zero crossing of the sine wave. In other words, the gating provides an exact "sine-wave" tone burst. Since the employed drive frequencies are 658 kHz to 659 kHz, the automatic adjustments to the burst width are on the order of a microsecond. The peak-to-peak voltage of the

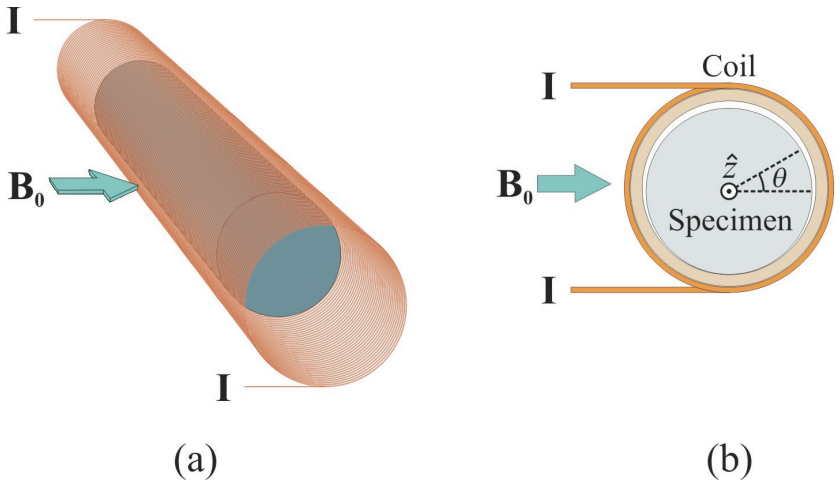

Figure 1: Configuration of coil, static magnetic field $\mathbf{B}_0$, and specimen: (a) 3D view and (b) cross-sectional view. The solenoid coil has 153 turns in a single layer wrapped around a Bakelite tube that is shown in (b) but not (a). The specimen is supported on one side along its length by the inside surface of the tube. An RF current $\mathbf{I}$ that passes through the coil induces opposing eddy currents around the perimeter of the specimen and, in the presence of $\mathbf{B}_0$, axially-directed Lorentz forces in opposite directions on the left and right sides of the specimen in (b).

burst at the output of the amplifier is (201 ± 2) V when loaded by the coil, specimen, and coaxial cable that connects the amplifier to the coil.

A block diagram of the electronic system is shown in Fig. 2. The output of the gated amplifier is passed through an active diplexer that connects the gated amplifier to the coil during the tone burst, while isolating the receiver and, then, connects the coil only to the input of the RAM-5000 receiver during free decay of resonant vibrations following the tone burst. This switching is controlled by a TTL gate that is generated by the RAM-5000.

The radio-frequency (RF) signal is passed through a filter with a band-pass of 0.05 MHz to 20 MHz. It is then passed through an intermediate frequency (IF) mixer, amplifier, and quadrature phase detector to extract time-dependent amplitudes of the in-phase component PhDet1 and out-of-phase component PhDet2 of the RF signal, relative to the reference sinusoid that was gated to generate the tone burst. The phase-detector outputs have a 50 kHz low-pass filter. The total gain in the electronic path from RF input to phase-detector output is (19.3 ± 0.2) dB. The digitized phase-detector

outputs are passed to a computer for analysis.

All parameters of signal acquisition and hardware processing are the same for measurements on the two specimens in this study, with the exception of the digitization rates, which are 6000 samples/s for Al-Zn and 4000 samples/s for Al-7075 (set differently because of less rapid decay during ringdown of Al-7075). To enable compensation for potential DC offsets in the baseline of the phase-detector outputs, waveform digitization is triggered before the beginning of the tone burst. 250 points before the tone burst are averaged to determine the baseline voltage.

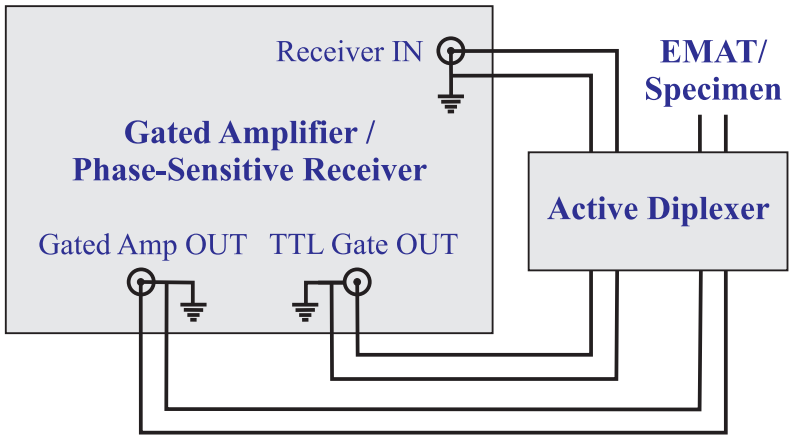

Figure 2: Configuration of electronics, electromagnetic transducer, and specimen.

4. Results

4.1. Resonant modes

In electromagnetic-acoustic transduction with Lorentz forces, the physical process of generation of dynamic forces in a metallic specimen involves (1) generation of an oscillating spatially-varying magnetic field vector $\mathbf{H}$ by a driving RF current $\mathbf{I}$ that passes through a coil winding of the transducer, (2) generation of eddy currents in the specimen by the time-dependent $\mathbf{H}$, (3) generation of Lorentz forces and associated momentum of electrons in the eddy currents in the presence of a static magnetic induction field $\mathbf{B}_0$, and (4) transfer of this force to the lattice through electron/ion collisions. The force density $\mathbf{f}$ in the specimen, as a function of cylindrical coordinates r, θ,

z, and time t', is given by [23]

$$\mathbf{f}(r,\theta,z,t') = \mathbf{J}_e(r,\theta,z,t') \times \mathbf{B}_0, \tag{1}$$

where $\mathbf{J}_e$ is the eddy current density.

With the geometry shown in Fig. 1, $\mathbf{I}$ is essentially parallel to the azimuthal unit vector $\hat{\theta}$ at each point in the coil, $\mathbf{B}_0$ is perpendicular to the coil axis $\hat{z}$, the dynamic $\mathbf{H}$ is predominantly parallel to $\hat{z}$ near the surface of the specimen [23], eddy currents at each point in the specimen are approximately parallel to $\hat{\theta}$, and Lorentz-forces are approximately parallel to $\hat{z}$. Therefore, Eq. 1 is closely approximated by

$$\mathbf{f}(r,\theta,z,t') = [\hat{\theta} \cdot \mathbf{J}_e(r,\theta,z,t')]|\mathbf{B}_0|(\cos\theta)\hat{z}, \tag{2}$$

where the dot product is almost independent of θ.

This force distribution couples to resonant vibrational modes with displacements predominantly in the $\hat{z}$ direction and phase variation of 2π around the circumference. In other words, the transducer excites modes with "axial-shear" displacements [24, 25]. An analysis of detailed displacement patterns and frequencies of these modes in finite cylinders is deferred to a subsequent study. For our purposes here, it is sufficient to note that these modes are similar to modes at cutoff in infinite isotropic cylinders (*i.e.,* with zero axial wavenumber) with purely axial displacements. In both geometries, the modes are doubly degenerate in the absence of transverse anisotropy. The displacement pattern of each member of the degenerate pair is shifted in its azimuthal dependence by 90° relative to that of the other member of the pair. In infinite cylinders, the resonant angular frequencies ω are solutions of [26]

$$J_1(\eta) - \eta J_2\eta) \;\; = \;\; 0, \tag{3}$$

where

$$\eta \equiv \omega a / v_s, \tag{4}$$

$J_{\rm n}$ is the Bessel function of the first kind of order n, a is the radius of the cylinder, and v_s is the velocity of axially polarized shear waves. Resonant modes with frequencies between 658 kHz and 659 kHz, which correspond to the second-lowest solution of Eq. 3 with $\eta = 5.33144$ and two radial nodes in the displacement pattern (including a node at $r = 0$), are employed in

this study. From these frequencies, η, and the measured specimen diameters, the shear velocities are estimated to be 3.1 mm/μs, consistent with typical ultrasonic shear velocities reported for pure and alloyed aluminum (e.g., [27, 28]).

In real polycrystalline cylinders, the degeneracy of axial-shear modes is split, due to transverse material anisotropy and/or azimuthal variation in diameter. In specimens Al-Zn and Al-7075, the fractional frequency splitting of the modes corresponding to $\eta = 5.33144$ is found to be 0.17 % and 0.05 %, respectively. Each mode of the nearly degenerate pair can be selectively excited by adjusting the azimuthal orientation of the specimen relative to $\mathbf{B}_0$ to maximize coupling to this mode while minimizing coupling to the other mode in the pair, despite the fact that the bandwidth of the driving tone burst is greater than the difference in the frequencies of the two modes.

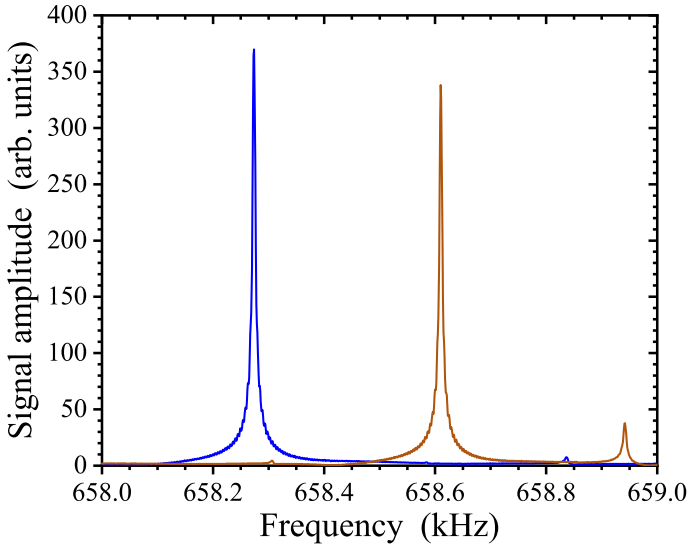

Figure 3: Frequency spectra of Al-7075 acquired with the azimuthal orientation of the specimen, relative to the direction of $\mathbf{B}_0$, tuned to optimize excitation of either the lower-frequency mode (blue curve) or higher-frequency mode (red curve) of the axial-shear pair corresponding to $\eta = 5.33144$.

Resonant spectra of Al-7075 between 658 kHz and 659 kHz with selective excitation of each of the modes corresponding to $\eta = 5.33144$ are shown in Fig. 3. The azimuthal tuning before acquisition of each of these spectra was accomplished by twisting the coil around its axis, with the specimen inside, until the signal from one of the axial-shear resonances was close to

zero with the driving frequency close to that resonance. The spectra were acquired by stepping the driving tone-burst frequency in increments of 1 Hz and, at each frequency, integrating each of the phase-detector outputs and computing the square root of the sum of squares of these two integrals. When the reference frequency of the tone burst is equal to a resonant frequency, this calculated value is approximately equal to the integrated magnitude of the combined output from the phase detectors. When the reference is offset from a resonance but the bandwidth of the tone burst provides some level of excitation of the resonance, the integrals of each of the phase detector outputs is reduced by oscillations (beats arising from the difference in the resonant and reference frequencies), and this effect leads to spectral peak widths similar to those expected from the measured logarithmic decrement of the signal ringdown.

One thing to note in Fig. 3 is the small unidentified peak near 658.94 kHz, which appears in the spectrum when the azimuthal orientation is set to maximize the higher of the two axial-shear modes. The coupling to this mode leads to slightly greater interference (beats) in time-domain signals during ringdown with excitation of the higher-frequency axial-shear mode. A similar situation of greater interference occurs in measurements of the higher-frequency axial-shear mode of Al-Zn. Because of this effect, the lower-frequency axial-shear mode in both specimens is employed to illustrate the time-domain measurement technique.

4.2. Waveform acquisition and initial analysis

The initial procedure employed for analysis of phase-detector waveforms includes compensation for receiver nonlinearity and time-dependent background subtraction. Nonlinearity of the receiver and relative gain imbalances of the two phase-detector channels were determined through measurements that employed a series of levels of continuous sinusoidal inputs as input to the receiver, with the RF frequency slightly offset from that of the internally generated reference sinusoid to provide sinusoidal outputs from the phase detectors. The resultant data on phase-detector output *vs.* amplitude of the RF input were fit to an an eighth-order polynomial, and this fit is used to compensate for instrument nonlinearity in all acquired waveforms.

Small time-dependent voltages are present after a tone burst, even in the absence of a specimen, because of finite recovery times of electronic components. To enable compensation for this effect, waveforms without a specimen in the coil are acquired and fit to a sum of two exponential decay functions

plus a constant, and this fit is subsequently subtracted from all waveforms acquired with a specimen in the coil. The detailed procedure for determining the background functions for each phase detector is described in the Appendix. The background phase-detector voltages are -4 mV to -2 mV immediately after the tone burst and decay to magnitudes less than 1 mV after 100 ms.

Fig. 4 shows an example of a pair of phase-detector waveforms from specimen Al-Zn after excitation at 658.70 kHz. These data are adjusted for receiver nonlinearity, and, then, time-dependent backgrounds (also corrected for receiver nonlinearity) are subtracted. Apart from these corrections, the data in this figure are raw acquired data. In other words, they are not derived from a digitized RF signal and are, instead, the output from analog signal processing.

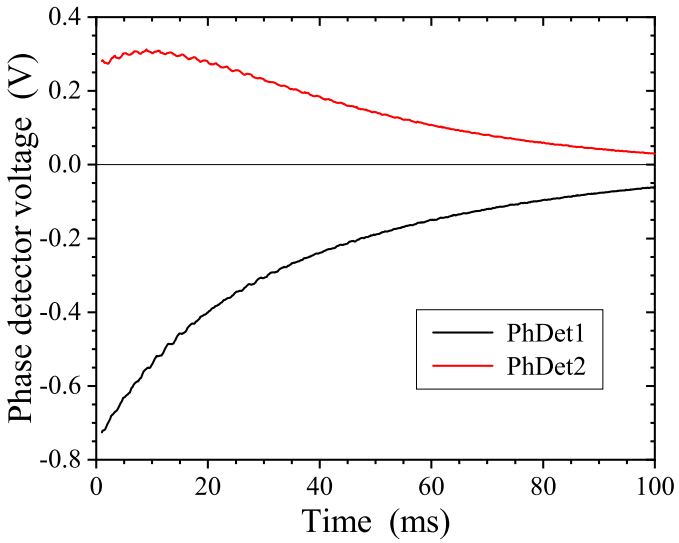

Figure 4: Phase-detector voltages *vs.* time, corrected for receiver nonlinearity and time-dependent background, from a waveform during ringdown of Al-Zn after tone-burst excitation at 658.70 kHz. The zero of time is defined as the end of the tone burst.

The instantaneous phase $\phi(t)$ of the RF signal relative to the reference sinusoid during ringdown is given by

$$\phi(t) = \tan^{-1}(PhDet2(t)/PhDet1(t)), \tag{5}$$

and the corresponding RF signal amplitude $A(t)$ before amplification by the

receiver, is given by

$$A(t) = 10^{-G_{\mathrm{dB}}/20}(PhDet1^2 + PhDet^2)^{1/2}, \tag{6}$$

where G_{dB} is the receiver gain in dB. Neglecting voltage drops in the cables and diplexer, $A(t)$ is equal to the RF voltage on the coil during ringdown. Fig. 5 shows ϕ and $A(t)$ *vs.* t extracted from the pair of phase-detector waveforms in Fig. 4 through the use of Eqs. 5 and 6.

The RF amplitude in Fig 5(b) shows small oscillations in voltage *vs.* time with amplitudes that are approximately 1 mV at the beginning of the waveforms and decay with time afterwards. These oscillations, which are also reflected in the phase-detector waveforms (Fig. 4) and phase (Fig 5(a)), arise from weak excitation of two unidentified resonant modes that are $\sim$ 420 Hz and $\sim$ 490 Hz above the dominant axial-shear mode. The amplitude of the oscillations are approximately 1.2 % of the RF amplitude of the dominant axial-shear mode, corresponding to $\sim$ 0.014 % of the excitation energy going into excitation of the unidentified modes.

To reduce noise in further waveform analysis, 50 pairs of phase-detector waveforms are acquired and separately processed in the sequence described above, and the extracted values for ϕ and RF amplitude *vs.* t are averaged. The automated acquisition of these 50 waveforms takes approximately 5.6 min. During this acquisition, the temperature of the specimen changes slightly. This leads to shifts in resonant frequency between waveforms, due to thermal expansion or contraction and intrinsic temperature dependence of acoustic velocities. Before acquisition of each waveform in the 50-waveform sequence, the excitation frequency is automatically tuned in real time to approximately match the current resonant frequency. This is accomplished with a technique involving calculation of the resonant frequency from the average slope of the relative signal phase *vs.* time over a user-specified interval (*e.g.*, 100 ms for Al-Zn) without adjusting signals for receiver nonlinearity or time-dependent background [29]. The relationship of resonant frequency to the slope of phase *vs.* time is described in more detail, below, in the context of extracting amplitude-dependent frequency shifts during ringdown. The maximal drift in frequency during the acquisition of each set of 50 waveforms in this study is 8 Hz (fractionally, 12 ppm). From published values of the thermal expansion coefficient and temperature dependence of the shear velocity of aluminum [27, 30], this frequency shift is estimated to arise from a temperature shift of approximately 0.04 °C.

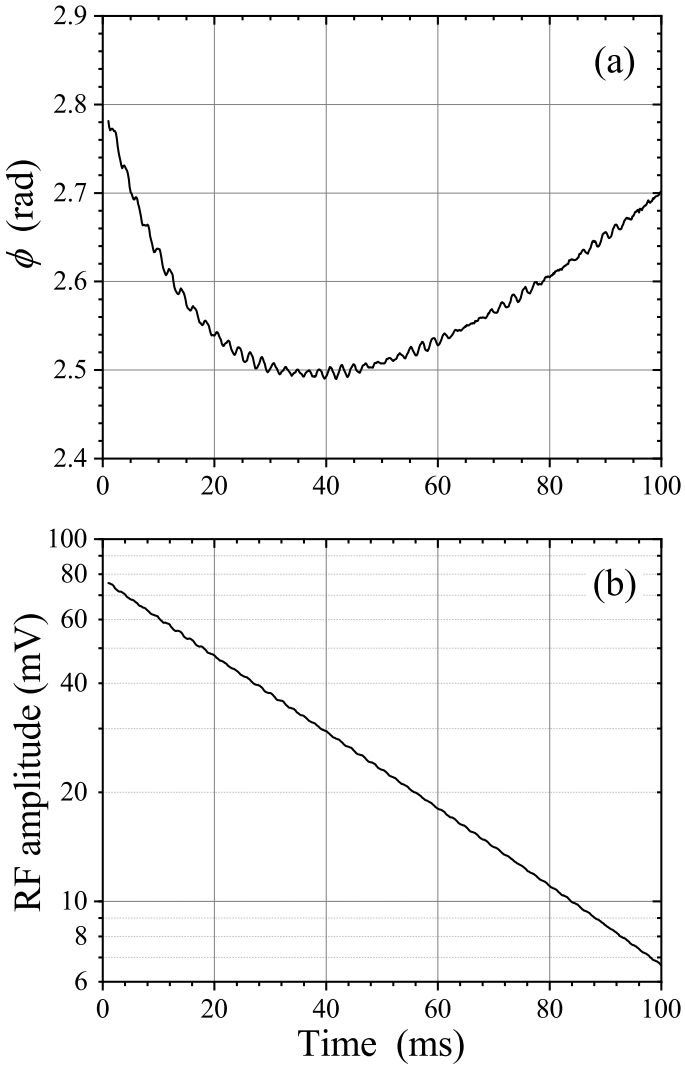

Figure 5: (a) Phase ϕ and (b) RF amplitude *vs.* time determined from the phase-detector waveforms from Al-Zn in Fig. 4

4.3. Resonant frequency during ringdown

A tone burst has a finite bandwidth given by the Fourier transform of the gated sine wave. Specifically, if the gated frequency of a sine-wave burst is f_{ref}, the bandwidth of the excitation is closely approximated by a sinc function with its first pair of minima at $f_{\mathrm{ref}} \pm 1/T_0$, where T_0 is the duration of the tone burst. If a resonance is within the bandwidth of a driving tone burst, it will be excited and, following the tone burst, decay at the resonant frequency, not f_{ref}. The instantaneous resonant frequency can also change during ringdown, because of nonlinear dependence on vibrational amplitude, and measurements of this effect are the focus of all NRS techniques.

The approach employed here for determining the instantaneous resonant frequency $f(t)$ takes advantage of the relation between this frequency, the reference frequency, and the derivative of the phase with respect to time t [31]:

$$\frac{d\phi(t)}{dt} = 2\pi[f(t) - f_{\mathrm{ref}}]. \tag{7}$$

Neglecting the small time-dependent oscillations in phase discussed in Sec. 4.2, the slope of $\phi(t)$ *vs.* t in Fig. 5(a) and the corresponding average $\phi(t)$ *vs.* t from 50 waveforms is not constant, indicating that the resonant axial-shear frequency changes as the RF amplitude decreases during ringdown.

Analysis of the data of averaged $\phi(t)$ *vs.* t proceeds by incrementally fitting these data to determine the time-dependent slope at each point in the waveform. A Savitzky-Golay smoothing algorithm with incremental second-order-polynomial fitting of windows of 100 points is employed, and this largely cancels the effect of the unidentified-mode interference. With the average of the set values of f_{ref} known, the extracted slope is converted through the use of Eq. (7) to a corresponding time-dependent resonant frequency $f(t)$.

This approach for determining time-dependent resonant frequency is innovative. While time dependence of phase determined by RITEC systems has been employed for measuring resonant frequencies in our labs at NIST for almost three decades, such measurements, until recently, neglected the time dependence of resonant frequencies during the period of a single ringdown. In other words, specimens were approximated as elastically linear, so that $d\phi/dt$ in Eq. 7 was approximated as constant during a single ringdown and f was determined from a linear least-squares fit of ϕ *vs.* t [29]. This approach with an approximation of linear elasticity is, in itself, unusual with RITEC

systems, which more commonly are employed in a stepped-frequency mode when measuring resonant spectra (as in Fig. 3).

The entire sequence of data acquisition and analysis, described above, is performed on four additional sets of 50 waveforms from Al-Zn to provide information on repeatability. Figure 6(a) shows an average of the results for fractional frequency shifts *vs.* RF amplitude obtained from the five sets of data, referenced to the frequency f_0 at an RF amplitude of 10 mV, and Fig. 6(b) shows the corresponding average RF amplitude *vs.* time. The resonant frequency at the beginning of ringdown is (658.689 ± 0.014) kHz (where the uncertainty corresponds to the range of values from the five data sets). Figure 6(a) indicates that the frequency increases by $\sim$ 6.2 ppm from the beginning of ringdown to the time in the ringdown where the amplitude is 10 mV. The error bars in this plot correspond to +/- two times the standard deviation σ of the five values of $(f\text{-}f_0)/f_0$ at the highest RF amplitude. All of the five values are within the range of these error bars.

Figure 6 also shows data obtained in a similar manner from five sets of 50 waveforms acquired from specimen Al-7075. At an RF amplitude of 82 mV, the magnitude of $(f\text{-}f_0)/f_0$ obtained from this specimen is $\sim$ 2 % of that obtained from specimen Al-Zn and is opposite in sign. The resonant frequency at the beginning of ringdown is (658.304 ± 0.021) kHz. The range of the error bars ($\pm 2\sigma$, ± 0.036 ppm) on the highest-amplitude point in this plot is approximately equal to half the diameter of the plotted symbols and shows that the values of $(f\text{-}f_0)/f_0$ differ significantly from zero at RF amplitudes greater than $\sim$ 55 mV.

As described in the previous section, each set of 50 waveforms is acquired over a period of several minutes, and there were slight temperature-dependent shifts in resonant frequency and f_{ref} from one waveform to the next. The specific sequence described here for the averaging of each set of 50 waveforms is designed to eliminate this effect in the final result for average $(f\text{-}f_0)/f_0$. Accurate results would not, for example, be obtained by directly averaging 50 pairs phase-detector waveforms, because the waveforms change from one ringdown to the next as a result of shifting resonant and reference frequencies. $\phi(t)$ extracted from each waveform has a linear term in the time dependence, corresponding to a constant term in $(f(t) - f_{\mathrm{ref}})$ for that waveform. With values of ϕ *vs.* t extracted separately from each waveform before averaging, the linear contribution to the average ϕ *vs.* t from a set of waveforms is given by the difference of the average constant contributions to $f(t)$ and average f_{ref} of the set of waveforms. Note that this linear contribution does not affect

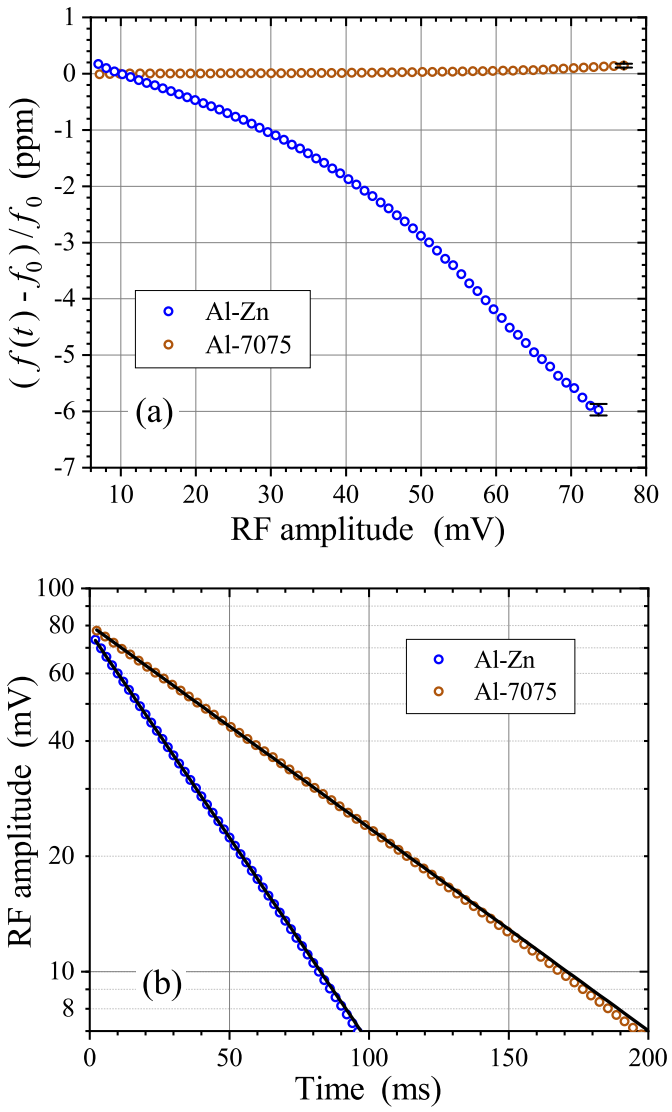

Figure 6: Average results from five sets of 50 waveforms for (a) fractional change in instantaneous resonant frequency $f(t)$ *vs.* RF amplitude, referenced to the frequency f_0 at an RF amplitude of 10 mV, and (b) RF amplitude *vs.* time during ringdown. Error bars in (a) correspond to $\pm 2\sigma$ of the highest-amplitude points points from the five data sets.

the amplitude dependence of the fractional frequency shifts plotted in Fig. 6, since it is removed by referencing the shifts to the frequency at a specified RF amplitude.

Before the acquisition of each set of 50 waveforms, the azimuthal orientation of the specimen was changed and, then, realigned to achieve approximately maximal signal amplitude. Therefore, the scatter in results from these sets and associated error bars in Fig. 6 include uncertainty in the process of manually maximizing the signal as a function of azimuthal angle.

4.4. Instrumental error in frequency shifts

Potential sources of error in the results presented in Fig. 6 also include drift in the RITEC reference frequency and phase-detector electronics during the 200 ms acquisition interval following tone-burst excitation. This issue is of greatest interest with respect to the results for Al-7075 in Fig. 6(a), because the measured frequency shifts for this sample are so small. To explore the magnitude of such contributions to systematic errors in time-dependent frequency shifts, tests were performed with a high-stability continuous-wave frequency source providing input to the diplexer (*i.e.*, replacing the signal from the EMAT/Specimen in Fig. 3.2) and with the high-voltage tone burst of the gated amplifier turned on but not connected to the diplexer. For this purpose, a Hewlett Packard 8662A signal generator was employed.

The sequence of data acquisition and analysis described in Secs. 4.2 and 4.3 was performed with the signal generator providing a sine wave at 658.0 kHz (close to the axial-shear resonant frequencies of samples Al-Zn and Al-7075) and an RF amplitude of 70.2 mV at the input to the diplexer. As described in Sec. 4.2, the acquisition and analysis included averaging of 50 waveforms with the RITEC reference frequency automatically adjusted before each waveform to approximately match the signal frequency (which, in this case, was constant). Such sets of waveforms were acquired repeatedly over a period extending from 3 hours to 6 hours after turning on the RITEC system and HP 8662A signal generator. This time period after turning on the instruments is similar to that employed in the measurements of Al-7075. At the beginning of this period, extracted frequencies were found to increase with time during the 200 ms acquisition interval during ringdown: a linear least-squares fit of these data found a statistically significant slope of $(2.02 \pm 0.07) \times 10^{-5}$ ppm/ms. Analysis of subsequent data sets shows that the slope during ringdown decreased to $(-2.98 \pm 0.06) \times 10^{-5}$ ppm/ms at the end of the test (6 hours after the instruments were turned on). This final

value corresponds to a fractional frequency shift of −0.006 ppm during the 200 ms interval of ringdown. Additional analysis shows that omitting the subtraction of background waveforms (described in Sec. 4.2) had no significant effect on the fit slope of the frequency shifts *vs.* time (within the stated uncertainty).

These tests of the stability of the RITEC reference frequency and phase detectors show that instrumental uncertainty in frequency shifts during ringdown are significant but smaller than other sources of uncertainty that contribute to the measurement variations between data sets indicated by the $\pm 2\sigma$ error bars in Fig. 6. In addition, the results of these tests indicate that the total frequency shift of 0.14 ppm measured for Al-7075 during ringdown does not arise from instrumental instability.

4.5. Logarithmic decrement

Values of the log decrement δ of Al-Zn and Al-7075 are determined to be $(3.75 \pm 0.01)\times10^{-5}$ and $(1.85 \pm 0.01)\times10^{-5}$, respectively, from linear least-squares fits on a semi-log scale1 of the data in Fig. 6(b) that have RF amplitudes greater than 20 mV. The data points in this fit were equally weighting on the log scale. These fits, extended to an RF amplitude of 7 mV, are plotted in this figure. The RF amplitudes immediately after the tone burst are determined from the fits to be (76.90 ± 0.05) mV and (80.4 ± 0.1) mV for Al-Zn and Al-7075, respectively.

5. Discussion

5.1. Precision

The error bars in Fig. 6(a) indicate a precision of ± 0.10 ppm and ± 0.04 ppm in the highest-amplitude data points for $(f\text{-}f_0)/f_0$ of Al-Zn and Al-7075, respectively, based on $\pm 2\sigma$ of values extracted from the five data sets from each specimen. These precisions are approximately two orders of magnitude better than the best reported fractional precision of 10 ppm for NRUS measurements [32]. Greater repeatability of the NRS measurements is understood to arise primarily from information on amplitude dependence being entirely contained within each waveform, which decays much more rapidly than the time scale required for NRUS measurements and, therefore, has less temperature-related uncertainty.

Specifically, as described in Sec. 4.1, the maximal fractional frequency drift during the 5.6 min interval employed here to acquire a set of 50 waveforms is found to be 12 ppm, and, for aluminum, this corresponds to a temperature drift of approximately 0.04 °C. The temperature drift during a 200 ms time interval of an individual waveform (such as those acquired for Al-7075) is estimated to be smaller by a factor approximately equal to the ratio of this interval to the acquisition time of the entire 50-waveform sequence: on the order of 2×10^{-5} °C. This corresponds to a temperature-related frequency drift of approximately 0.01 ppm. The order-of-magnitude greater uncertainty of $\pm\,0.10$ ppm indicated by the $\pm\,2\sigma$ error bars for Al-Zn in Fig. 6(a) is understood to arise from other sources, most likely dominated by irreproducibility in azimuthal alignment of the specimen and associated variations in electromagnetic-acoustic coupling strength.

In contrast, NRUS measurements require acquisition of multiple stepped-frequency spectra with different drive amplitudes, and such measurements are significantly affected by ambient time-dependent temperature variations [32]. To accurately measure resonance spectra in NRUS, the dwell time at each frequency in the spectrum must be great enough to essentially achieve the CW excitation level (*i.e.*, substantially greater than the time to drop to 1/e in exponential decay). Therefore, the time required to acquire a single NRUS spectrum is greater than that of a single NRS measurement by a factor greater than the number of frequency steps in the NRUS spectrum, and acquisition of multiple NRUS spectra at different drive amplitudes takes much longer. To address this issue, Pasqualini *et al.* [33] implemented an NRUS system with long-term temperature stability of 10^{-2} °C, leading to frequency stability on the order of $\pm\,100$ ppm in measurements near 1 kHz. Haupert *et al.* [32] established an approach involving, for each specimen, repeated acquisition of low-amplitude reference spectra before acquisition of each spectrum at a higher drive level, and they reported frequency precision on the order of 10 ppm in measurements on several materials. To our knowledge, this is the best precision reported for NRUS measurements.

Other NRS techniques also offer the advantage of minimal temperature drift during measurements of amplitude dependence of resonant frequencies. However, the precision of NRS measurements does not appear to be reported in published studies, which have focused predominantly on audio and sub-audio frequencies. Relative to these other NRS techniques, the technique presented here offers further advantages of noise reduction through super-heterodyne and phase-sensitive reception. Specifically, phase-sensitive (lock-

in) reception enables low-pass hardware filtering of the phase of the signal, relative to the reference sinusoid, providing information on changes in resonant frequency on a relevant time scale during ringdown (e.g., on the order of several milliseconds in the examples presented here), rather than requiring software analysis of noisier RF signals acquired with digitization rates greater than the resonant frequency.

The number of waveforms (50) employed here in the data averaging sequence was chosen arbitrarily, and the dependence of uncertainty of the results on this number has not yet been not explored. In light of the hypothesis offered in the previous section that scatter in values of $(f\text{-}f_0)/f_0$ (error bars in Fig. 6(a)) is dominated by irreproducibility of azimuthal alignment of specimens, it seems likely that the number of acquired waveforms and associated acquistion times could be substantially reduced without much effect on uncertainties.

5.2. Transduction efficiency

The measured RF signal amplitudes in Fig. 6(b) are proportional to the instantaneous vibrational amplitudes in the specimens during ringdown. Since both specimens are aluminum, the electromagnetic-acoustic transduction efficiency and associated constants of proportionality between the signal amplitudes and vibrational amplitudes are expected to be close to the same for the two specimens, so that Figure 6(a) provides information on the relative dependence of resonant frequencies on vibrational amplitude.

The validity of the approximation of equal transduction efficiencies for these specimens is considered by comparing the ratio of the measured RF amplitudes at the beginning of ringdown with an estimate of this ratio based on the logarithmic decrement and material properties. The resonant vibrational amplitude $A_{\mathrm{cw}}(\vec{z})$ at an arbitrary point $\vec{z}$ within a resonator subjected to a continuous-wave (CW) sinusoidal excitation at the resonant frequency is proportional to the resonator quality factor Q (equal to π/δ [34]) and inversely proportional to the effective elastic stiffness [35]. In the specific case of CW excitation of an axial-shear mode, the corresponding elastic stiffness is ρv_s^2 [36], where ρ is density and $v_s = \omega a/\eta$ (Eq. 3). From the measured values of a, ω, ρ, and δ of Al-Zn and Al-7075 (Secs. 2 and 4.3), the ratio of the resonant vibration amplitude of Al-Zn to that of Al-7075 with equal CW electromagnetic-acoustic excitation is expected to be approximately 0.51. The dominant factor contributing to this ratio is δ, and the 0.02 % difference in v_s has an insignificant effect.

With tone-burst excitation at a resonant frequency, the vibrational amplitude $A(\vec{z}, t')$ of a linear resonator during excitation is a superposition of the solution of the equation of motion with CW excitation and a time-dependent solution in the absence of excitation, with the prefactor of the time-dependent part selected to match the initial condition of $A(\vec{z}, 0) = 0$ (where time t' is defined to be zero at the beginning of the tone burst). If δ is approximately constant during ringdown, $A(\vec{z}, t')$ increases with time towards the CW level:

$$A(\vec{z}, t') = A_{\mathrm{cw}}(\vec{z}) \left[1 - \exp\left(-\frac{\omega t' \delta}{2\pi} \right) \right]. \tag{8}$$

This equation leads to an estimate of the vibrational amplitude of Al-Zn at the end of a 2.6 ms tone burst that is approximately 1.017 times greater than that of Al-7075. The reason that this ratio is slightly greater than 1, even though the CW amplitude of Al-Zn is smaller than that of Al-7075, is the greater ρ of Al-7075 and the approximate cancellation of the effect of δ when $t' \ll 2\pi/\omega\delta$. The amplitudes would be predicted to be approximately equal if the tone burst had a duration of 5 ms.

The actual measured RF amplitude from Al-Zn at the end of the tone burst (determined from the logarithmic fit of RF amplitude *vs.* time in Fig. 6(b)) is (4.3 ± 1.9)% less than that from Al-7075 (where the indicated uncertainty is based on 2σ of the amplitudes from the five data sets for each specimen). This 5.9 % discrepancy between predicted and measured signal levels of Al-Zn, relative to Al-7075, corresponds to a $(3.0 \pm 0.9)\%$ difference in the one-way electromagnetic/acoustic coupling efficiency for the two samples.

One factor that has not been considered, thus far, in estimating the relative received RF amplitudes is a difference in electrical conductivity. Al-Zn is expected to have higher conductivity than Al-7075 because of its lower concentration of alloying elements, and this difference is reflected in a measured impedance of the coil plus connecting BNC cable that is (1.5 ± 0.1 %) lower with Al-Zn inserted in the coil than with Al-7075 inserted. This slightly lower impedance will lead to an increase in the current in the coil with the fixed V_0 that is employed in the measurements. For a given coil current, the conductivity dependence of the conversion efficiency between the current and the force on the sample is expected to be insignificant. Specifically, Thompson [37] showed theoretically and Gaerttner *et al.* [38] showed experimentally (for shear plane waves) that differences in specimen conductivity have an insignificant effect on this conversion efficiency if the ratio of

the electromagnetic skin depth to the acoustic wavelength is much less than 1. The axial-shear modes in aluminum near 658 kHz in this study are well within this regime of acoustic wavelength relative to skin depth. As explained by Thompson [37], the reason for this insensitivity to conductivity in highly conducting metals at low ultrasonic frequencies is that the magnitude of the total RF current in the specimen per unit surface area (integral of the current density *vs* depth) is independent of conductivity. Therefore, the higher driving coil current with Al-Zn is predicted to lead to a slightly ($\sim$ 1.5 %) greater excitation force on the specimen and a corresponding increase in the discrepancy between the predicted and measured signal amplitudes of Al-Zn, relative to Al-7075.

As described in Sec. 4.3, beats in the RF amplitude from Al-Zn during ringdown (Fig. 5 (b)) indicate that a fraction of the excitation energy ($\sim$ 0.014 %) is channeled into excitation of two unidentified modes. Similar beats are present in waveforms from Al-7075 (arising from excitation of a mode $\sim$ 560 Hz above the dominant axial-shear mode, which is visible near 658.84 kHz in Fig. 3), but the amplitude of these beats is approximately 1/3 of those observed in the signals from Al-Zn. The greater fraction of excitation energy being channeled into unidentified modes in Al-Zn is not great enough to explain the discrepancy in the measured and predicted signal amplitudes from this specimen.

In the absence of other viable explanations for the discrepancy of several percent in measured and predicted relative signal amplitudes, we are apparently left with the possibility that a difference in the resonant vibrational patterns of the two specimens affects the degree to which the Lorentz forces (with spatial dependence given by Eq. 2) match the vibrational patterns and, therefore, affects the transduction efficiency. The measured modes of these specimens are nominally the same types of "axial-shear" modes, as evidenced by the fact that they are each one of two overwhelmingly dominant nearly-degenerate modes in the frequency range expected for axial-shear modes with $\eta = 5.33144$ (Eq. 3) in homogeneous transversely isotropic aluminum cylinders. However, differences in material homogeneity or anisotropy would lead to differences in resonant vibrational patterns and associated matching of these patterns to the driving axial Lorentz forces (Eq. 2). An hypothesis of greater transverse inhomogeneity or anisotropy and associated reduction in coupling strength in Al-Zn is supported by the fact that the splitting of the frequencies of the two nominally degenerate axial-shear modes is approximately four times greater in Al-Zn than in Al-7075 (Sec 4.1).

5.3. Noncontacting electromagnetic-acoustic transduction

Contacting piezoelectric transducers have been reported to introduce irreproducibility in nonlinear measurements [39] and frequency shifts in linear RUS measurements [40]. The noncontacting electromagnetic-acoustic transduction method employed here to demonstrate phase-sensitive NRS measurements offers the advantage of essentially eliminating nonlinearity and acoustic loss associated with mechanical contact.

5.4. Physical source of nonlinearity

A detailed analysis of physical mechanisms responsible for the amplitude dependence of resonant frequencies shown in Fig. 6(a) is beyond the scope of this study. However, a couple of points about the interpretation of these data should be briefly noted.

In a previous study of nonlinearity of additively manufactured 17-4 stainless steel specimens with various levels of built-in porosity [21], we suggested that dislocations are the dominant contribution to amplitude dependence of resonant frequencies observed in phase-sensitive NRS measurements. This hypothesis is supported by the results in Fig. 6(a), which show the magnitude the nonlinearity of Al-7075 to be a factor of ~ 50 smaller than that of Al-Zn. The alloying-element concentration in Al-7075 is expected to be 55 to 80 times greater than that in Al-Zn (Sec. 2) and is, therefore, expected to produce greater pinning of dislocations and associated suppression of the dislocation contribution to nonlinear acoustic strain. The difference in acoustic loss in the two specimens (Fig. 6(b)) is also consistent with dislocations being the predominant source of loss in these materials, with anelastic motion of dislocations being more inhibited by pinning in Al-7075.

As in our previous measurements of 17-4 stainless steel, the resonant frequency of Al-7075 is found to increase with increasing vibrational amplitude (Fig. 6(a)). The sign of this dependence indicates the presence of higher-order nonlinear terms in the stress-strain relation (assuming classical nonlinearity), since the lowest-order nonlinear term (quadratic in strain) can only lead to frequencies decreasing at higher amplitudes [41]. The fact that Al-7075 and Al-Zn have opposite signs of amplitude-dependent frequency shifts, in addition to having much difference magnitudes of these shifts, indicates that the ratios of multiple nonlinear coefficients are different in these two specimens. This type of behavior and detailed functional forms of amplitude dependence are anticipated to be a focus of future work.

6. Conclusion

The NRS technique presented in this paper offers advantages, relative to previous NRS techniques, of a reduction in signal noise through phase-sensitive superheterodyne reception and a reduction in computational signal-processing effort. Digitization of signals from a vibrational sensor is bypassed through analog signal processing, while preserving all information on amplitude dependence of resonant frequencies during resonant decay. The specific hardware described here can be applied to resonant modes with frequencies as great as 20 MHz with no increase in computation time or complexity. The general measurement technique can also be implemented with instruments that operate at frequencies below the ultrasonic range, such as lock-in amplifiers without superheterodyne reception, enabling nonlinear acoustic characterization of large structural components.

The precision of measured fractional changes in frequency is found to surpass the best reported precision of nonlinear resonant ultrasound spectroscopy (NRUS) by two orders of magnitude, and this is attributed primarily to less temperature drift during resonant ringdown than that which occurs in intrinsically more time-consuming acquisition of stepped-frequency spectra. The technique is sensitive to multiple orders of nonlinearity, which are reflected in the detailed amplitude dependence of resonant frequency shifts, and, unlike propagating-wave harmonic-generation techniques, extraction of information on the contributions from multiple nonlinear terms in the stress-strain relation is not complicated by the frequency dependence of acoustic attenuation and diffraction.

The specific electromagnetic-acoustic transduction method employed here to demonstrate phase-sensitive NRS provides the additional advantage of noncontacting excitation and reciprocal detection of resonant vibrations. Although this method is employed here with a regular cylindrical geometry to enable clear identification of excited modes, it is readily applicable to more complex geometries. Therefore, phase-sensitive NRS with electromagnetic-acoustic transduction provides an attractive option for nondestructive detection of material variations in geometrically complex additively manufactured parts.

References

[1] M. B. Prime, D. W. Shevitz, Linear and nonlinear methods for detecting cracks in beams, Proc. 14th Intnl. Modal Analysis Conference

(1996) 1437–1443.

[2] K. E.-A. Van Den Abeele, A. Sutin, J. Carmeliet, P. A. Johnson, Micro-damage diagnostics using nonlinear elastic wave spectroscopy (NEWS), NDT&E Int. 34 (2001) 239–248.

[3] M. Muller, A. Sutin, R. Guyer, M. Talmant, P. Laugier, P. A. Johnson, Nonlinear resonant ultrasound spectroscopy (NRUS) applied to damage assessment in bone, J. Acoust. Soc. Am. 118 (2005) 3946–3952,

[4] P. Shokouhi, J. Riviere, C. R. Lake, P.-Y. Le Bas, T. J. Ulrich, Dynamic acousto-elastic testing of concrete with a coda-wave probe: comparison with standard linear and nonlinear ultrasonic techniques, Ultrasonics 81 (2017) 59-65.

[5] C. Espinoza, D. Feliú, C. Anguilar, R. Espinoza-González, F. Lund, V. Salinas, N. Mujica, Linear versus nonlinear acoustic probing of plasticity in metals: A quantitative assessment, Materials 11 (2018) 2217.

[6] K. M. S. Levy, J.-Y. Kim, L. J. Jacobs, Investigation of the relationship between classical and nonclassical ultrasound nonlinearity parameters and microstructural mechanisms in metals, J. Acoust. Soc. Am. 148 (2020) 2429.

[7] K. H. Matlack, J.-Y. Kim, L. J. Jacobs, J. Qu, Review of second harmonic generation measurement techniques for material state determination in metals, J. Nondestruct. Eval. 34 (2015) 273.

[8] F. Windels, K. Van Den Abeele, The influence of localized damage in a sample on its resonance spectrum, Ultrasonics 42 (2004) 1025–1029.

[9] K. E.-A. Van Den Abeele, P. A. Johnson, A. Sutin, Nonlinear elastic wave spectroscopy (NEWS) techniques to discern material damage, Part I: Nonlinear wave modulation spectroscopy (NWMS), Res. Nondestr. Eval. 12 (2000) 17–30.

[10] L. Pieczonda, A. Klepka, A. Martowicz, W. J. Staszewski, Nonlinear vibroacoustic wave modulations for structural damage detection: an overview, Opt. Eng. 55 (2016) 011005.

[11] A. Carcione, P. Blanloeuil, L. R. F. Rose, C. H. Wang, M. Veidt, J. Sound Vib. 446 (2019) 238–248.

[12] K. Van Den Abeele, P. Y. Le Bas, B. Van Damme, T. Katkowski, Quantification of material nonlinearity in relation to microdamage density using nonlinear reverberation spectroscopy: Experimental and theoretical study, J. Acoust. Soc. Am. 126 (2009) 963–972.

[13] B. Van Damme, K. Van Den Abeele, The application of nonlinear reverberation spectroscopy for the detection of localized fatigue damage, J Nondestruct. Eval 33 (2014) 263–268.

[14] D. Torello, S. Thiele, K. H. Matlack, J.-Y. Kim, J. Qu, L. J. Jacobs, Diffraction, attenuation, and source corrections for nonlinear Rayleigh wave ultrasonic measurements, Ultrasonics 56 (2015) 417–426.

[15] J. A. TenCate, New nonlinear acoustic techniques for NDE, AIP Conf. Proc. 557 (2001) 1229.

[16] Y. Yang, E. J. Ng, P. M. Polunin, Y. Chen, I. B. Flader, S. W. Shaw, M. I. Dykman, T. W. Kenny, Nonlinearity of degenerately doped bulk-mode silicon MEMS resonators, J. Microelectromech. S. 25 (2016) 859–868.

[17] J. M. Londoño, S. A. Neild, J. E. Cooper, Identification of backbone curves of nonlinear systems from resonance decay responses, J. Sound Vib. 348 (2015) 224–238.

[18] V. Ondra, I. A. Sever, C. W. Schwingshackl, A method for non-parametric identification of non-linear vibration systems with asymmetric restoring forces from a resonant decay response, Mech. Syst. Signal Pr. 114 (2019) 239–258.

[19] M. Feldman, Non-linear system vibration analysis using Hilbert transform – I. Free vibration analysis method "FREEVIB," Mech. Syst. Signal Pr. 8 (1994) 119–127.

[20] P. M. Polunin, Y. Yang, M. I. Dykman, T. W. Kenny, S. W. Shaw, Characterization of MEMS resonator nonlinearities using the ringdown response, J. Microelectromech. S. 25 (2016) 297–303.

[21] W. L. Johnson, J. F. Whiting, F. H. Kim, P. R. Heyliger, N. W. Hrabe, Resonant acoustic nonlinearity and loss in additively manufactured stainless steel, AIP Conf. Proc. 2102 (2019) 020008.

[22] International Alloy Designations and Chemical Composition Limits for Wrought Aluminum and Wrought Aluminum Alloys, Aluminum Association, Arlington, 2018.

[23] M. Hirao, H. Ogi, Electromagnetic Acoustic Transducers: Noncontacting Ultrasonic Measurements using EMATs, 2nd Edition, Springer Japan, 2017, p. 22.

[24] W. L. Johnson, G. A. Alers, Noncontacting ultrasonic resonance measurement of transverse anisotropy in cylinders, in Review of Progress in Quantitative Nondestructive Evaluation, Vol. 14, ed. D. O. Thompson, D. E. Chimenti, Plenum, New York, 1995, pp. 1915–1921.

[25] W. Johnson, G. A. Alers, Force measurement using vibrational spectroscopy, Rev. Sci. Instrum. 68 (1997) 102–108.

[26] A. C. Eringen, E. S. Şuhubi, Elastodynamics, Vol. II, Academic, New York, 1975.

[27] G. Simmons, H. Wang, Single Crystal Elastic Constants and Calculated Aggregate Properties: A Handbook, MIT, Cambridge, 1971.

[28] W. Johnson, B. A. Auld, G. A. Alers, Spectroscopy of resonant torsional modes in cylindrical rods using electromagnetic-acoustic transduction, J. Acoust. Soc. Am. 95 (1994) 1413–1418.

[29] W. Johnson, Ultrasonic resonance of metallic spheres at elevated temperatures, J. Phys. IV 6 (C8) (1996) 849–852.

[30] Metals Handbook Desk Edition, ed. J. R. Davis, CRC, Boca Raton, 1998.

[31] E. Rubiola, Phase Noise and Frequency Stability in Oscillators, Cambridge University Press, Cambridge, 2009, p. 6.

[32] S. Haupert, G. Renaud, J. Rivière, M. Talmant, High-accuracy acoustic detection of nonclassical component of material nonlinearity, J. Acoust. Soc. Am. 130 (5) (2011) 2654.

[33] D. Pasqualini, K. Heitmann, J. A. TenCate, S. Habib, D. Higdon, and P. A. Johnson, Nonequilibrium and nonlinear dynamics in Berea and Fontainebleau sandstones: Low-strain regime, J. Geomphys. Res. 112 (2007) B01204.

[34] A. S. Nowick, B. S. Berry, Anelastic Relaxation in Crystalline Solids, Academic, New York, 1972.

[35] A. P. French, Vibrations and Waves, Norton, New York, 1971, p. 88.

[36] B. A. Auld, Acoustic Fields and Waves in Solids, Vol. I, Krieger, Malabar, 1990.

[37] R. B. Thompson, Physical Principles of Measurements with EMAT Transducers, in Physical Acoustics, Vol. XIX, ed. R. N. Thurston and A. D. Pierce, Academic, Boston, 1990.

[38] M. R. Gaerttner, W. D. Wallace, B. W. Maxfield, Experiments Relating to the Theory of Magnetic Direct Generation of Ultrasound in Metals, Phys. Rev. 184 (1969) 702–704.

[39] S. Thiele, J.-Y. Kim, J. Qu, L. J. Jacobs, Air-coupled detection of nonlinear Rayleigh surface waves to assess material nonlinearity, Ultrasonics 54 (2014) 1470–1475.

[40] W. L. Johnson, C. F. Martino, S. A. Kim, P. R. Heyliger, Mode-selective acoustic spectroscopy of trigonal piezoelectric crystals, IEEE T. Ultrason. Ferr. 55 (2008) 1133–1142.

[41] A. H. Nayfeh, D. Mook, Nonlinear Oscillations, Wiley-VCH, Weinheim, 2004, p. 55.

7. Appendix

The following procedure is employed to determine the time-dependent background for each phase detector:

- 100 pairs of waveforms (PhDet1 and PhDet2 *vs.* time) are acquired with the excitation frequency fixed at a value approximately equal to the frequency of the specimen resonance.

- For each of these waveforms, the average voltage of points before the tone burst is subtracted and a correction for instrument nonlinearity is applied (using the polynomial-based correction factor, described in Sec. 4.2).

- The resultant waveforms are averaged to provide a single pair of background waveforms for PhDet1 and PhDet2 with reduced noise.

- The two averaged waveforms are separately fit to a sum of two exponential functions plus a constant. The statistical R^2 values of fits are 0.997 for PhDet1 and 0.988 for PhDet2, and the standard deviations of both fits are 0.05 mV.